Acta Oceanol. Sin., 2021, Vol. 40, No. 7, P. 77–87
https://doi.org/10.1007/s13131-021-1738-x
http://www.aosocean.com
E-mail: ocean2@hyxb.org.cn

Identification of the sensitive area for targeted observation to improve vertical thermal structure prediction in summer in the Yellow Sea

Huiqin Hu[1, 2†], Jingyi Liu[1, 2†], Lianglong Da[1, 2*], Wuhong Guo[1, 2], Kun Liu[2], Baolong Cui[1, 2]
[1] Navy Submarine Academy, Qingdao 266199, China
[2] Pilot National Laboratory for Marine Science and Technology (Qingdao), Qingdao 266237, China

Received 23 June 2020; accepted 27 August 2020

Abstract
The sensitive area of targeted observations for short-term (7 d) prediction of vertical thermal structure (VTS) in summer in the Yellow Sea was investigated. We applied the Conditional Nonlinear Optimal Perturbation (CNOP) method and an adjoint-free algorithm with the Regional Ocean Modeling System (ROMS). We used vertical integration of CNOP-type temperature errors to locate the sensitive areas, where reduction of initial errors is expected to yield the greatest improvement in VTS prediction for the selected verification area. The identified sensitive areas were northeast–southwest orientated northeast to the verification area, which were possibly related to the southwestward background currents. Then, we performed a series of sensitivity experiments to evaluate the effectiveness of the identified sensitive areas. Results show that initial errors in the identified sensitive areas had the greatest negative effect on VTS prediction in the verification area compared to errors in other areas (e.g., the verification area and areas to its east and northeast). Moreover, removal of initial errors through deploying simulated observations in the identified sensitive areas led to more refined prediction than correction of initial conditions in the verification area itself. Our results suggest that implementation of targeted observation in the CNOP-based sensitive areas is an effective method to improve short-term prediction of VTS in summer in the Yellow Sea.

Key words: targeted observation, sensitive area, vertical thermal structure (VTS), conditional nonlinear optimal perturbation (CNOP)

Citation: Hu Huiqin, Liu Jingyi, Da Lianglong, Guo Wuhong, Liu Kun, Cui Baolong. 2021. Identification of the sensitive area for targeted observation to improve vertical thermal structure prediction in summer in the Yellow Sea. Acta Oceanologica Sinica, 40(7): 77–87, doi: 10.1007/s13131-021-1738-x

1 Introduction

Continental shelf seas, at the interface between land and the marine environment, are dynamic shallow seas closely connected to human activities (MacKinnon and Gregg, 2005). Vertical thermal structure (VTS) is an important physical characteristic of continental shelf seas (MacKinnon and Gregg, 2003) that plays a vital role in the circulation pattern and biological systems of continental shelves and affects marine fishing, communication, submarine expeditions, and oceanic exploration (Jin et al., 1993). Thus, the accuracy of VTS prediction for continental shelf seas has drawn the attention of researchers and coastal communities. Moreover, the accuracy of short-term (7 d) VTS prediction, which includes detailed information about VTS, has particularly important practical application value, for example, it affects the use of acoustic instruments and deployment of fishing gear. Therefore, demand for accurate prediction of short-term VTS in continental shelf seas has increased in recent years.

The Yellow Sea is a semi-enclosed marginal sea and can be considered a typical shallow continental shelf sea (Fig. 1). Unlike the VTS in deep seas, which tends to follow the pattern of a mixed layer, thermocline, and deep layer, the VTS in shallow seas is dynamic and vulnerable to numerous forcing factors (Chu et al., 1997). This complicates short-term prediction, which requires a detailed description of VTS. Studies have indicated that the short-term VTS in the Yellow Sea is influenced by dynamic and thermodynamic processes at multiple temporal and spatial scales, such as the Yellow Sea Cold Water Mass (YSCWM) in summer, the solar diurnal radiation cycle, tides, and vertical mixing (Qiu, 1982). Additionally, the structure of the continental shelves in the Yellow Sea, such as the continental shelf over the selected area (denoted as Box A in Fig. 1b), is complex. Therefore, accurate prediction of VTS in the Yellow Sea is challenging.

It is known that the quality of numerical prediction is sensitive to the quality of the initial conditions (ICs) used (Bei et al., 2012; Hu et al., 2014; Majumdar, 2016; Mu, 2013; Mu et al., 2015, 2017); therefore, providing ICs with higher quality is potential to

---

Foundation item: The National Natural Science Foundation of China under contract Nos 41705081 and 41906005; the Innovation Special Zone Project under contract No. 18-H863-05-ZT-001-012-06; the Open Project Fund of the Laboratory for Regional Oceanography and Numerical Modeling, Pilot National Laboratory for Marine Science and Technology (Qingdao) under contract No. 2019A05.

*Corresponding author, E-mail: llda@qnlm.ac

†These authors contributed equally to this work.

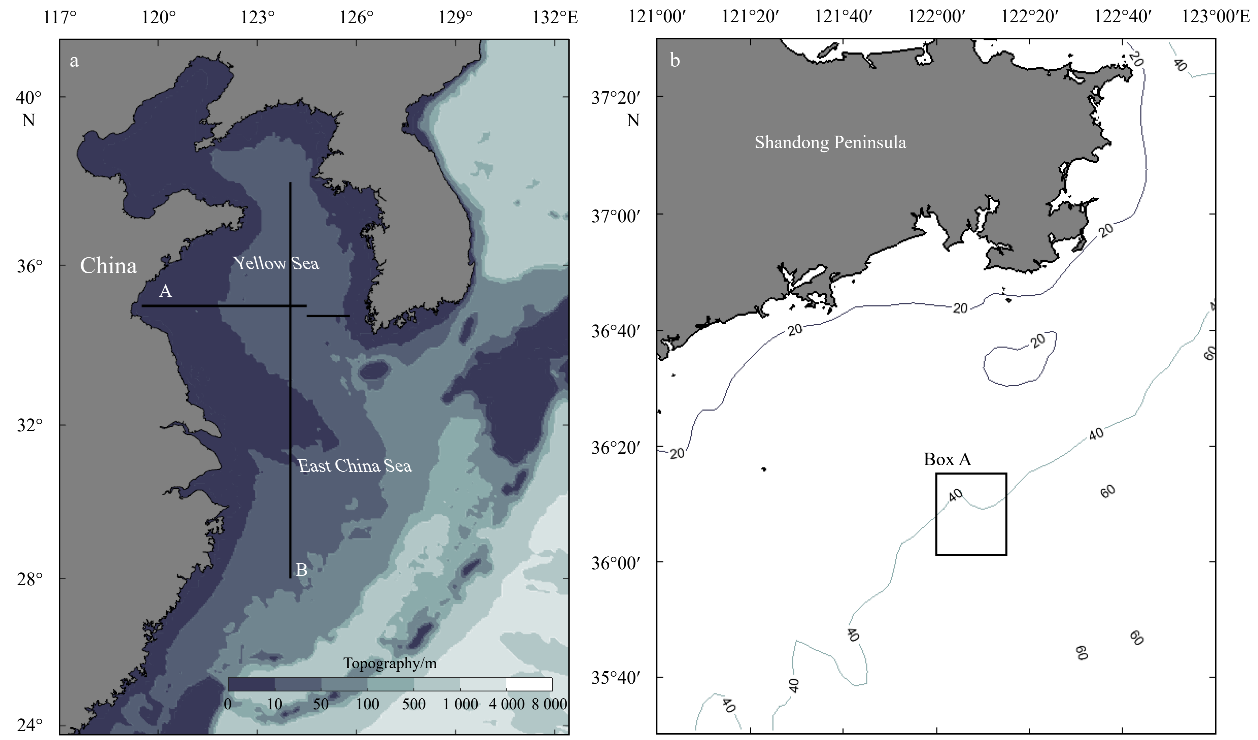

Fig. 1. Model domain and topography (depth, m) of model grids (a), and topography (m) of the mid-western part of the Yellow Sea (b). The black solid lines A and B in a indicate locations of the validation sections; the box with black solid line (Box A) in b indicates the location of the selected verification area.

improve the prediction of VTS. Assimilating available observations is a common approach to obtain higher quality ICs for numerical prediction (Hu et al., 2017a, b). Despite the substantial increase in available oceanic observations (e.g., satellite-derived and *in situ* observations) over the last few decades, observations remain sparse in certain focal areas. Furthermore, supplemental observations (in addition to those from existing observational networks) in the ocean are costly both during deployment and maintenance phases. Hence, observation strategies to determine where supplemental observations should be collected are urgently needed. Targeted (or adaptive) observation is a strategy with the goal of maximizing the reduction in forecast uncertainty of a numerical prediction model by implementing supplemental observations in areas where further observations are expected to improve forecasting (Langland, 2005; Palmer et al., 1998). These areas are commonly referred to as sensitive areas, because improvement of ICs in these areas through assimilation of supplemental observations is expected to provide a greater benefit to forecasting compared to other areas (Li et al., 2014).

Targeted observation was first introduced in atmospheric studies, and has provided great benefits in the form of improved numerical weather and climate predictions, such as forecasts of precipitation, snow storms and tropical cyclones (TCs), as well as El Niño-Southern Oscillation (ENSO) prediction (Hu and Duan, 2016; Huang and Meng, 2014; Morss et al., 2001; Qin and Mu, 2011). Subsequently, this strategy was applied in oceanic research, such as for Kuroshio-related forecasting, including the beginning of the Kuroshio, Kuroshio large meander (KLM), upstream Kuroshio transport, and Kuroshio extension, as well as forecasting of the ocean state in the region related to the South China Sea Western Boundary Current and forecasting of the Atlantic meridional overturning circulation (Baehr et al., 2008; Kramer et al., 2012; Li et al., 2014; Mu et al., 2015; Wang et al., 2013; Wen and Duan, 2019; Zhang et al., 2017). However, these marine studies have mainly focused on specific marine phenomena and have been conducted mainly in deep seas. To date, few studies have applied targeted observation for the content of marine VTS prediction, especially in shallow continental shelf seas such as the Yellow Sea.

A vital issue in targeted observation studies is the identification of sensitive areas. Several strategies have been developed to identify such areas. One strategy employs an ensemble technique such as the ensemble transform Kalman filter (Bishop et al., 2001) or the ensemble Kalman filter (Hamill and Snyder, 2002). Another strategy is based on the adjoint technique, for example, using singular vectors (Palmer et al., 1998), adjoint sensitivities (Ancell and Mass, 2006), and the adjoint-derived sensitivity steering vector (Wu et al., 2007). In recent years, the conditional nonlinear optimal perturbation (CNOP) method, first proposed by Mu et al. (2003), has drawn increasing attention from researchers. This method identifies the most rapidly developing perturbations in a nonlinear system, thus can be used as a nonlinear approach to identify the sensitive areas in a nonlinear forecast system. The CNOP method has been successfully applied to identify the sensitive areas for improving the prediction of atmospheric and oceanic phenomena, such as ENSO, TCs, and KLM (Duan et al., 2004, 2018; Tan and Wang, 2010; Wang et al., 2013). However, the application of the CNOP method generally relies on the adjoint technique, which requires complex coding and a large computational cost (Liang et al., 2019; Zhang et al., 2017). To realize the advantages of the CNOP method while avoiding the adjoint technique, Wang and Tan (2009) proposed an adjoint-free fast algorithm to determine the CNOP based on an empirical orthogonal function (EOF), hereafter referred as the EOF-

CNOP algorithm (a detailed description of this algorithm is provided in Section 2). By applying the EOF-CNOP algorithm, promising results have been obtained for TC forecasting using an operational regional forecast model in China (Wang and Tan, 2009). As noted above, short-term VTS is affected by physical processes at multiple temporal and spatial scales. This complexity means that a nonlinear method of identifying sensitive areas has the potential to provide more reasonable results for targeted observation. Thus, the EOF-CNOP algorithm was employed for targeted observation of short-term VTS prediction in this study. Then, two interesting questions should be raised: How can sensitive areas be identified for short-term VTS prediction using the EOF-CNOP algorithm? How effective are the identified sensitive areas for short-term VTS prediction?

To answer these questions, the EOF-CNOP algorithm was applied with the Regional Ocean Modeling System (ROMS) model, which is widely applied for regional oceanic simulation and forecasting (Yang et al., 2011; Zhang et al., 2017). Additionally, because stratification of the VTS is stronger in summer than in other seasons in the Yellow Sea (Zhang et al., 2006), this study focused on the VTS of the Yellow Sea in summer. The outline of this paper is as follows. Section 2 introduces the model setup and briefly describes the EOF-CNOP algorithm. The detailed experimental design and results of sensitivity experiments are presented in Section 3. Discussion and a summary are provided in Section 4.

2 Model and methods

2.1 *Model setup*

This study employed the Rutgers version of the ROMS model to simulate the thermocline distribution and circulation structure of the Yellow Sea. The ROMS model is a three-dimensional, free-surface, vertical terrain-following nonlinear numerical model containing a series of horizontal diffusion and vertical mixing parameterization schemes (Shchepetkin and McWilliams, 2005). In this study, we selected the harmonic horizontal mixing (Wajsowicz, 1993) and K-profile parameterization schemes (Large et al., 1994) to calculate horizontal diffusion and vertical mixing, respectively.

The model domain is from 23.7°N to 41.3°N and 117°E to 132.5°E (Fig. 1a), with a horizontal resolution of (1/24)°. It contains 506 meridional grid points, 372 zonal grid points, and 32 vertical levels, which are refined in the upper ocean with the stretching parameter θ_s=6. The minimum water depth in the nearshore region and the maximum water depth were set to 10 m and 6 000 m, respectively. Input data for bottom topography were obtained from the smoothed topographic dataset ETOPO2 (https://ngdc.noaa.gov/mgg/global/etopo2). The initial temperature and salinity fields and open boundary conditions were obtained from multiyear averaged (1998–2018) HYCOM+NCODA reanalysis data (https://www.hycom.org/dataserver). The surface forcing factors, including wind stress, heat flux, and water exchange, were derived from multiyear averaged (1998–2018) ECMWF Re-Analysis-interim data (https://apps.ecmwf.int/datasets/).

ROMS was integrated for 25 model years from a cold start, with both the initial velocity and free-surface elevation set to zero. The model must reach a stable state before its results can be analyzed. Based on the result of temporal evolution of kinetic energy (KE) over the whole domain, it could be found that the initial KE developed quickly and reached a quasi-equilibrium state after a spin-up period of about 5 model years. Therefore, model output of climatological simulation for the last 20 model years were used for all analyses in this study.

2.2 *CNOP approach and calculation*

In general, the governing equations of ROMS can be expressed as:

$$\begin{cases} \dfrac{\partial \boldsymbol{X}}{\partial t} + \mathrm{F}(\boldsymbol{X}) = 0 \\ \boldsymbol{X}|_{t=0} = \boldsymbol{X}_0 \end{cases}, \tag{1}$$

where F is a nonlinear partial differential operator and $\boldsymbol{X}$ represents the state vectors of nonlinear model state variables. $\boldsymbol{X}_0$ represents the initial state vector of $\boldsymbol{X}$ at time t=0.

The numerical solution of Eq. (1) at forecast time t can be expressed as follows:

$$\boldsymbol{X}_t = \mathrm{M}_t(\boldsymbol{X}_0), \tag{2}$$

where $\boldsymbol{X}_t$ is the nonlinear evolution of the initial state vector $\boldsymbol{X}_0$ at time t, which was set to 7 d in this study. M is a discrete nonlinear propagation operator of F, which is used to propagate $\boldsymbol{X}_0$ to $\boldsymbol{X}_t$.

Thus, the nonlinear evolution of the initial perturbation $\delta\boldsymbol{x}$ at forecast time t can be expressed as:

$$\delta\boldsymbol{x}_t = \mathrm{M}_t(\boldsymbol{X}_0 + \delta\boldsymbol{x}) - \mathrm{M}_t(\boldsymbol{X}_0). \tag{3}$$

According to the definition of CNOP by Mu et al. (2003), for a chosen norm $||\cdot||$, the initial perturbation $\delta\boldsymbol{x}^*$ is referred to as the CNOP with a constraint condition of $||\delta\boldsymbol{x}|| \leqslant \beta$ only if

$$\mathrm{J}(\delta\boldsymbol{x}^*) = \max_{||\delta\boldsymbol{x}|| \leqslant \beta} (\mathrm{J}(\delta\boldsymbol{x})) = \max_{||\delta\boldsymbol{x}|| \leqslant \beta} ||\mathrm{M}_t(\boldsymbol{X}_0 + \delta\boldsymbol{x}) - \mathrm{M}_t(\boldsymbol{X}_0)||, \tag{4}$$

where $\mathrm{J}(\delta\boldsymbol{x})$ is the objective function used to estimate the nonlinear evolution of $\boldsymbol{X}_0$ at the forecast time, and β is the constraint of the initial perturbation $\delta\boldsymbol{x}$. Thus, CNOP represents the initial perturbations with the maximum amplitude of nonlinear evolution under the given constraint conditions over a certain time interval.

The normal process of determining CNOP relies on the adjoint technique for calculating the gradient of the objective function. As noted in Section 1, to avoid the complex coding and large computational cost when using the adjoint technique, we applied the EOF-CNOP algorithm in this study. The basic concept of the EOF-CNOP algorithm is as follows: first, the initial perturbation sets x' are employed to generate the corresponding prediction increment sets y' through numerical integration. Then, EOF decomposition is used to obtain the orthogonal basis of the initial perturbation sets. Then, a statistical relationship model can be established between x' and y'. Finally, the gradient of the objective function in the iteration of the optimization process can be calculated to obtain the CNOP.

In practice, before calculating CNOP, the form of objective function and initial constraint conditions should be set according to the focused study object. Because this study focused on VTS, the objective function was defined as the change of predicted vertically-integrated temperature in specified verification area (denoted as A) caused by initial perturbations in the specified sensitive area. Note that the initial perturbations were only added on the temperature field. The objective function can be expressed as follows:

$$\mathrm{J} = \iiint_{\mathrm{A}} \left(T_t{'}\mathrm{d}x\mathrm{d}y\mathrm{d}z \right)^2 = \iiint_{\mathrm{A}} \left[(T_t(t_0 + t^{'}) - T_t(t_0))\mathrm{d}x\mathrm{d}y\mathrm{d}z \right]^2, \tag{5}$$

where $T_t^{'}$ is the change of predicted vertically-integrated temperature at time t caused by the initial temperature perturbation t'. t_0 is the initial state of temperature. The initial constraint conditions over the whole model domain D is expressed as (Li et al., 2014):

$$||\delta t||^2 = \iiint_{\mathrm{D}} \left(\frac{t^{'}}{t_{\mathrm{sd}}} \right)^2 \mathrm{d}x\mathrm{d}y\mathrm{d}z \leqslant \beta^2, \tag{6}$$

where t_{sd} represents the area-averaged standard deviation of temperature over the area of domain D. This standard deviation of temperature was calculated from the statistical mean of the World Ocean Atlas 2018 (WOA18, https://www.nodc.noaa.gov/OC5/woa18) in August, and set to 0.25 in this study. The constraint radius β was set to 2.5×10^3 to ensure the stability of model integration, and keep the vertically-integrated temperature changes caused by initial perturbations in an appropriate range. After determining the objective function and the initial constraint conditions, we utilized the sequential quadratic programming (SQP) algorithm (Powell, 1983) to calculate CNOP.

3 Results

3.1 *Model validation*

To validate model results in the study area, we first compared the spatial distributions of the simulated sea surface temperature (SST) in different seasons with that from observations (Fig. 2). The simulated monthly averaged SST in February, May, August, and November were selected to represent the predicted situations in winter, spring, summer, and autumn, respectively. The multi-year averaged SST from 1985 to 2001 from the satellite data of the Moderate-resolution Imaging Spectroradiometer (MODIS) were used as the observations.

In general, both the seasonal thermal variations of sea surface in simulation and the spatial distribution of simulated SST in each season were in good agreement with that from the MODIS data. Specifically, due to the seasonal variations of solar radiation and winds, SST was low in winter, high in summer, and SST values in autumn and spring fell between those in winter and summer in the Yellow Sea. These seasonal variations of SST were well reproduced by both the simulation and MODIS data. Additionally, SST in the East China Sea continental shelf and the Yellow Sea in winter (also in other three seasons) were much lower than those in the Kuroshio area on the East China Sea slope, which is possibly related to the transportation of warm water from low latitude to high latitude due to Kuroshio travelling along the East China Sea slope from south to north. The simulated spatial thermal differences of sea surface between the Kuroshio area and other areas corresponded well with that from the MODIS data. Note that, due to the limitation of model horizontal resolution and defects in the regional prediction model at open boundaries, the detailed SST spatial structures resolved by the MODIS data were not captured by simulation in some areas, such as nearshore and open boundary regions. However, this model still has some skills of simulating the temporal and spatial thermal variations on sea surface, especially for analyses in the

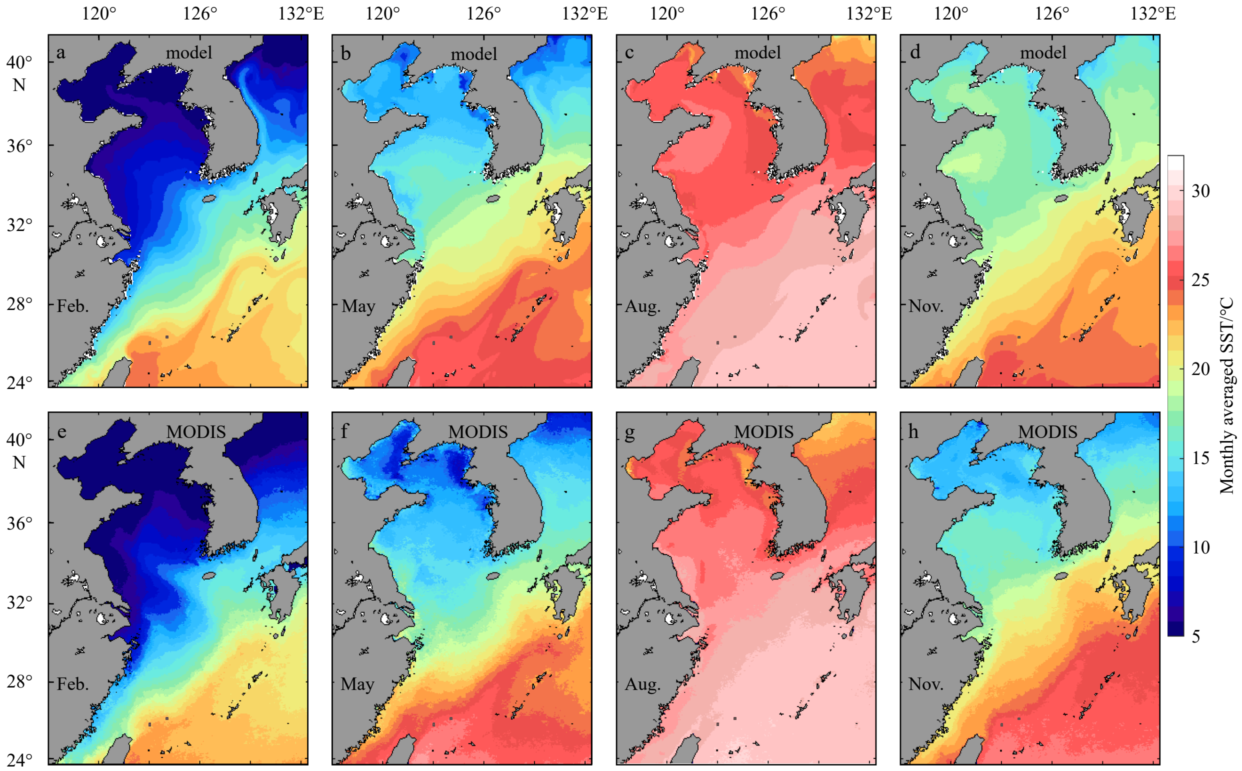

Fig. 2. Monthly averaged SST in February, May, August, and November (from left to right) from the climatological simulation of model (upper row, a–d), and the multi-year averaged SST in the corresponding months from the satellite data of MODIS (bottom row, e–h).

study area.

Furthermore, to validate the simulation of summertime VTS in the Yellow Sea, we selected two typical vertical sections, a section at 35°N (solid line A, Fig. 1a) and a section at 124°E (solid line B, Fig. 1a). Along these two vertical sections, the simulated monthly averaged temperature in August were compared with that from observations obtained from the Atlas of Ocean Data in the China seas (Chen et al., 1992).

The simulated thermal structure along these two vertical sections were generally consistent with those from the ocean atlas (Fig. 3). Specifically, water in summer is well-mixed in the shallow Yellow Sea due to the strong solar radiation and weak horizontal wind, and stratified near the central basin (Zhang et al., 2006). The vertical distribution of isothermals corresponded well for the observation and simulation. Additionally, below the thermocline, the general shape of the YSCWM, one of the most important water masses in the summertime Yellow Sea, was well reproduced by both the observation and the simulation. Note that, further study is still required to improve the accuracy of simulated VTS, especially below the upper mixed layer.

3.2 *Identification of CNOP-based sensitive area*

Identifying sensitive area is a vital issue for targeted observation. In this study, we attempted to identify sensitive area in targeted observation for predicting short-term (7d) summertime VTS in the specified verification area using EOF-CNOP algorithm (noted in Section 2.2). The VTS in the region of Box A (Fig. 1b) is influenced by thermodynamic and dynamic processes and complex topography (noted in the introduction section), which leads to large prediction uncertainties of VTS in this region (Xia et al., 2006). Therefore, this region, which approximately covers an area of 0.24°×0.25° (36.02°–36.26°N, 122.00°–122.25°E; Box A in Fig. 1b), was selected as the verification area in this study. Given that this study was conducted based on climatological simulation (noted in Section 2.1), we selected three different cases (listed in Table 1) of climatological stable states to repeat procedure of identifying sensitive areas with aiming to ensure universality of the identified sensitive areas.

According to Wang and Tan (2009), to identify the sensitive area, an initial ensemble consisting of a reference IC without perturbations and 27 ICs with random temperature perturbations was generated for each case. The reference IC without perturbations, which is from the stable climatological run (noted in Section 2.1), was regarded as the true IC (denoted as IC_{true}). The initial random perturbations of temperature were generated for the whole domain and satisfied the normal distribution $N(0, \sigma)$, where σ is 0.25 based on the statistical results provided in WOA18. Then, we calculated the CNOP for each case using this initial ensemble of 28 ICs and their corresponding 7-d predictions. After calculating the CNOP, the guidance should be defined to identify sensitive areas. Previous studies have shown that different guidances should be utilized for different physical processes (Tan et al., 2010; Zhou and Zhang, 2014; Zhang et al., 2016, 2017). Given that we only focused on identifying the two-dimensional (horizontal) sensitive areas and the practical issue of VTS, similar to the guidance used by Zhang et al. (2017), the vertically integration temperature scheme was employed as the guidance for sensitive area identification in this study. In this scheme, the sensitive area was defined as the region of horizontal grid points, where the CNOP-type errors have the vertically integrated temperature to full water depth higher than a certain value τ. The value of τ was selected to make the size of the sensitive area equal to that of the verification area, which contained 56 horizontal model grids in this study. Thus, the distribution of CNOP-type errors can generally correspond to locations of the identified sensitive area.

Figure 4 displays distributions of vertically integrated temperature for the CNOP-type errors, which reflected locations of the identified sensitive areas as noted above, for the three cases. Given that we focused on the relative importance of CNOP-type er-

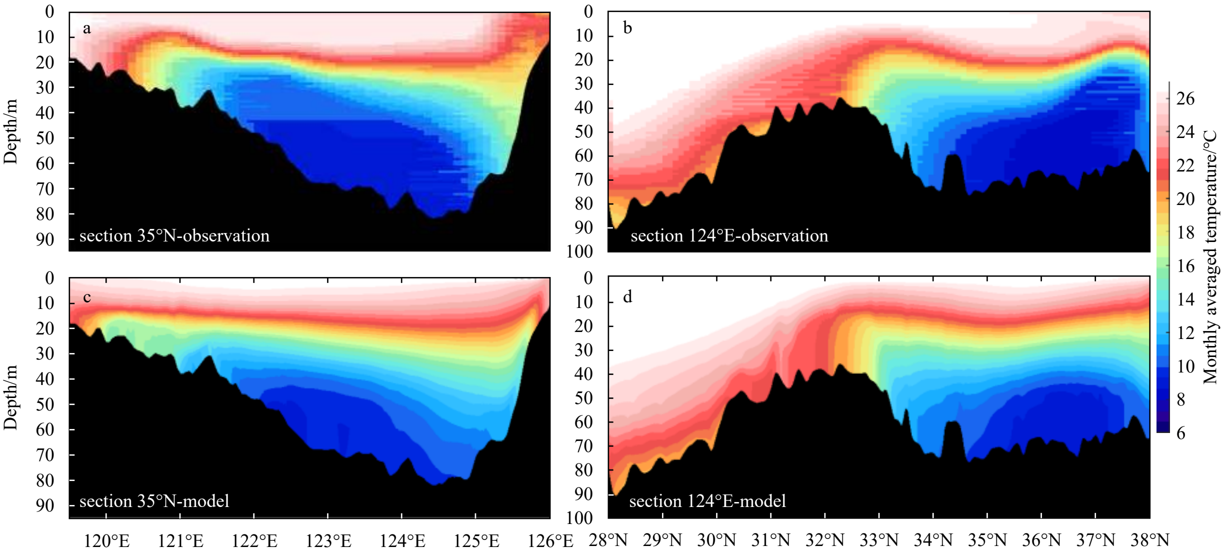

Fig. 3. Vertical sections of monthly averaged temperature in August along 35°N (left column, a, c) and 124°E (right column, b, d), for observation from ocean atlas data (upper row, a, b) and model simulation (bottom row, c, d).

Table 1. Three different cases for identifying sensitive areas

	Case 1	Case 2	Case 3
Initial time	August of the 21st year	August of the 23rd year	August of the 25th year

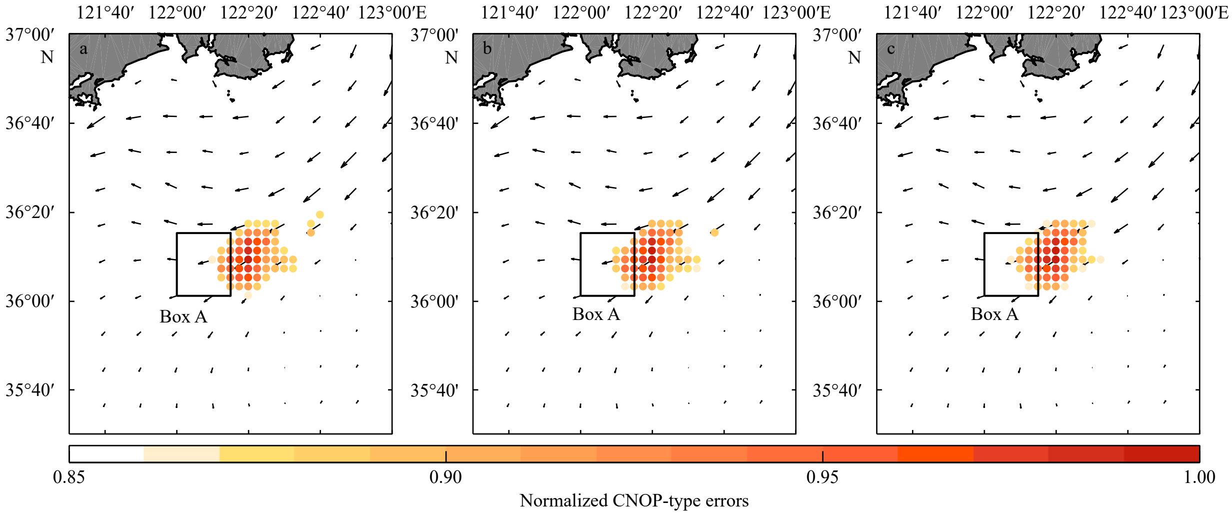

Fig. 4. Locations (colored dots) of the identified sensitive areas and the climatological background currents (vectors) for cases of the 21st (a), 23rd (b) and 25th (c) climatology years, respectively. The sensitive areas are identified based on CNOP-type errors of vertically-integrated temperature after being normalized with their maximum values.

rors among the whole domain when identifying sensitive area in this study, the CNOP errors were normalized based on their maximum value. Although the precise corresponding model grid positions of sensitive areas for these three cases differed, the distributions of sensitive areas in these three cases were generally consistent. Specifically, the identified sensitive areas were generally northeast-southwest orientated, with most portion of the sensitive areas located to the east of the verification area (Box A in Fig. 1b) and small portion located in the verification area. Additionally, high values in the identified sensitive areas, which represents areas with relatively greater importance for VTS prediction, were mainly concentrated to the east of the verification area. The orientation of the identified sensitive areas agreed well with that of the background currents (Fig. 4), which implies that the CNOP-type errors were possibly related to the background currents. Because the identified sensitive areas for these three cases were similar, only results for Case 3 were used in the following analyses.

3.3 *Validation of CNOP-based sensitive area*

According to the definition of CNOP, we can infer that the initial perturbations in the CNOP-based identified sensitive area will cause the largest errors for VTS prediction in the verification area at the verification time compared to perturbations in other areas. To verify this speculation, we conducted a set of sensitivity experiments (listed in Table 2) as follows: first, we generated a set of local random initial temperature perturbations. The method of generation perturbation is similar to that described in Section 3.2 except that perturbations were generated over specified local areas with the same grid size of the verification area instead over the whole domain. Then, we added initial random perturbations on four different areas to the $\mathrm{IC}_{\mathrm{true}}$, respectively. These four areas were the verification area, two areas related to the background currents (an area to east of the verification area and an area to northeast of the verification area), and the sensitive area (locations shown in Figs 5a1, b1, c1 and d1), respectively. Finally, corresponding to those four ICs, four simulations were conducted and their prediction errors of temperature were compared. The prediction errors were calculated based on simulation from the $\mathrm{IC}_{\mathrm{true}}$ (denoted as True Run).

Table 2. Sensitivity experiments based on adding initial random perturbations

Experiment name	Initial conditions	Location of adding perturbations
True Run	$\mathrm{IC}_{\mathrm{true}}$	no
Exp_A_1	$\mathrm{IC}_{\mathrm{true}}$	verification area
Exp_A_2	$\mathrm{IC}_{\mathrm{true}}$	sensitive area
Exp_A_3	$\mathrm{IC}_{\mathrm{true}}$	east of the verification area
Exp_A_4	$\mathrm{IC}_{\mathrm{true}}$	northeast of the verification area

Figure 5 shows the horizontal distributions of temperature prediction errors at water depth of 20 m at different prediction times for experiments with adding initial random perturbations on different areas. For experiment with initial random perturbations added on the verification area itself (Exp_A_1), the errors were highly significant in the verification area at the initial time, but gradually decreased as prediction time increased. At the verification time, prediction errors in the verification area, although exist, were much smaller compared to the original state. For experiment with initial random perturbations added on the identified sensitive area (Exp_A_2), initial errors gradually propagated into the verification area as prediction time increased. At the verification time, the prediction errors generally propagated into the verification area, and were larger than prediction errors caused by initial random perturbations added on the verification area itself. The initial random perturbations added on the other two areas (Exp_A_3 and Exp_A_4) had limited impacts on prediction errors in the verification area. In particular, initial random perturbations added on the area northeast of the verification area (Exp_A_4) had no notable impact on the prediction errors for the verification area at the verification time. Similar results were obtained at other water depths (figures not shown). Note that initial perturbations both on the verification area and on the identified sensitive areas propagated approximately southwestward, which could also imply that the identified sensitive areas were possibly related to southwestward background currents upstream the verification area (mentioned in Section 3.2).

Further, to quantitatively investigate the effect of initial random perturbations in the identified sensitive area on VTS predic-

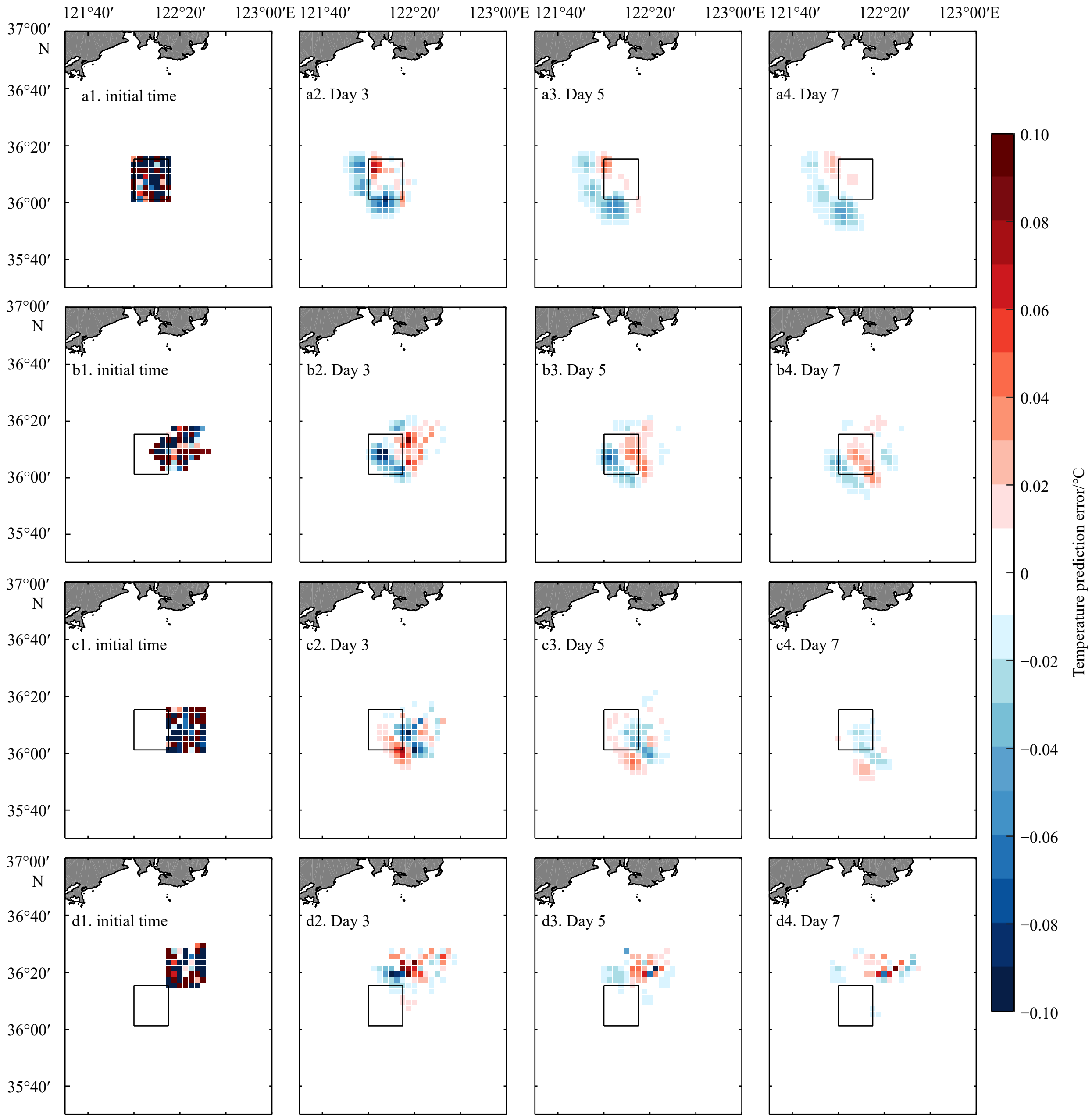

Fig. 5. Temperature prediction errors (shaded) at water depth of 20 m over the verification area for experiments with adding initial random perturbations on four different areas at four different prediction times. Four different areas are the verification area (Exp_A_1, a1–4), sensitive area (Exp_A_2, b1–4), area to east of the verification area (Exp_A_3, c1–4), and area to northeast of the verification area (Exp_A_4, d1–4), respectively. Four different prediction times are the first, third, fifth and seventh prediction day, respectively.

tion in the verification area, we compared the temporal evolutions of area-averaged root mean square error (RMSE) of temperature profiles over the verification area for those four experiments. The RMSE is calculated as follows:

$$\mathrm{RMSE} = \sqrt{\frac{1}{N}\sum_{i=1}^{N}\left(\theta_i - \hat{\theta}_i\right)^2}, \quad (7)$$

where θ_i and $\widehat{\theta}_i$ are the predicted temperature profile at each model grid in the verification area for experiments with and without initial random perturbations, respectively. N is the total number of model grids in the verification area.

The effects of initial random perturbations in different areas on the prediction of VTS in the verification area differed (Fig. 6). For experiment with adding initial perturbations on the verification area (Exp_A_1), the RMSE at initial time was larger compared to initial perturbations added on other areas, but decreased with increasing forecasting time. For experiment with initial perturbations added on the sensitive area (Exp_A_2), the RMSE at initial time was not zero because the sensitive area partially overlapped with the verification area. With increasing forecasting time, RMSE of this experiment gradually exceeded that of the experiment with adding initial perturbations on the verification area (Exp_A_1), and became the largest at the seventh pre-

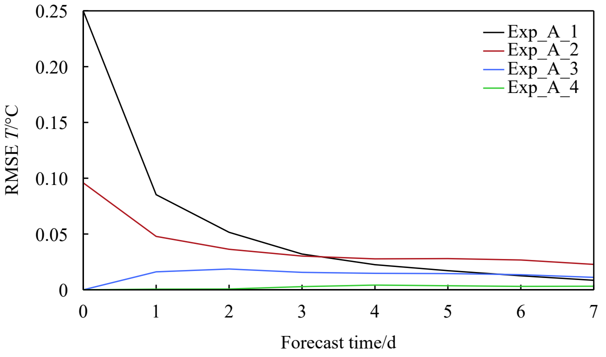

Fig. 6. Temporal evolution of root mean square errors of area-averaged temperature profile over the verification area for experiments with adding initial random perturbations on the verification area (Exp_A_1, black line), sensitive area (Exp_A_2, red line), area to east of the verification area (Exp_A_3, blue line), area to northeast of the verification area (Exp_A_4, green line), respectively.

diction day among these four experiments. For experiments with adding initial perturbations on the area to east of the verification area (Exp_A_3) and the area to northeast of the verification area (Exp_A_4), RMSEs for both of these two experiments were zero at the initial time, and smaller than the experiment with adding initial perturbations on the sensitive area (Exp_A_2) at the seventh prediction day. These results indicate that initial random perturbations of temperature added on the sensitive area rather than other areas developed into the largest changes in the verification area within the prediction period of 7 d, and thus had the greatest negative impact on predictions of VTS in the verification area. Therefore, identification method used in this study could be considered as effective for identifying sensitive areas for VTS prediction.

3.4 *Effectiveness of targeted observation*

As noted in Section 3.3, initial errors added on the sensitive areas defined by CNOP developed much larger in the verification area than initial errors added on other areas. This implies that removing initial errors from the CNOP-based sensitive areas has potential to improve VTS prediction (Zhang et al., 2019). To investigate whether targeted observation in the identified sensitive areas could effectively improve prediction of VTS in the verification area, we performed another set of sensitivity experiments (listed in Table 3). The detailed experimental design was as follows. First, output from True Run was regarded as simulated observations. Then, we generated initial random perturbations of temperature over the entire model domain with method similar to that described in Section 3.2, and added them to IC_{true} to obtain a new IC (denoted as IC_{pg}). The model run started from IC_{pg} was denoted as Ctrl Run. In addition to Ctrl Run, runs with IC_{pg} in the verification area and the identified sensitive area being replaced by IC_{true} were denoted as Exp_R_1 and Exp_R_2, respectively. Note that, IC_{pg} in the verification area being replaced by IC_{true} could be considered as removing initial errors (improving ICs) from this area through deploying simulated observations of temperature profile in this area. Thus, Exp_R_1 was same as the Control Run except that initial errors (ICs) in the verification area were removed (improved) due to simulated observations deployed in the verification area. Exp_R_2 was same as Exp_R_1 except that simulated observations were deployed in the identified sensitive area. Based on these experiments, we can measure the effects of simulated observations in different areas on performance of VTS prediction.

Table 3. Sensitivity experiments based on removing initial random errors

Experiment name	Initial conditions	Location of removing initial random errors (replace IC_{pg} with IC_{true})
True Run	IC_{true}	no
Ctrl Run	IC_{pg}	no
Exp_R_1	IC_{pg}	verification area
Exp_R_2	IC_{pg}	sensitive area

Figure 7a shows the temporal evolutions of area-averaged temperature RMSE over the verification area for experiments with removing initial errors from different areas through deploying simulated observations. We can see that at the end of 7-d prediction period, the prediction errors over the verification area was greatly reduced by experiment with deploying simulated observation in the identified sensitive area (Exp_R_2) than that of experiment without deploying simulated observations (Ctrl Run) and experiment with simulated observations being deployed in the verification area itself (Exp_R_1). This indicates that targeted observation in the identified sensitive area was effective for improving 7-d prediction of VTS in the verification area.

Besides of the prediction errors evaluated above, it is important to directly evaluate the prediction improvement brought by removing initial errors. To quantitatively assess the prediction improvement induced by assimilating simulated observations in different areas, we calculated the prediction benefits as documented in Zhang et al. (2019), which was expressed as:

$$P = \frac{dT_1 - dT_2}{dT_1} \times 100\%, \tag{8}$$

where $dT_1 = |T_{\text{Ctrl Run}} - T_{\text{True Run}}|$ and $dT_2 = |T_{\text{Replacing Run}} - T_{\text{True Run}}|$ are the absolute area-averaged temperature RMSE over the verification area in Ctrl Run and Replacing Run (Exp_R_1 and Exp_R_2), respectively.

Figure 7b shows the prediction benefits of experiments with removing initial errors from different areas. Removing initial errors from the verification area and the identified sensitive area both improved the prediction of VTS. Moreover, removing initial errors from the identified sensitive area brought more benefits for improved VTS prediction than that from the verification area itself. This further proves the effectiveness of targeted observation in the identified sensitive area for improving 7-d VTS prediction of VTS in the verification area.

It should be noted that when ICs in different areas were simply replaced with that of IC_{true}, the issue of imbalance in the initial state should be considered. Similar to the experimental design documented in Li et al. (2014), four experiments of 7-d VTS prediction were conducted with different ICs (Table 4) under the same boundary conditions and forcing (documented in Section 2.1). We calculated biases of the predicted temperature between experiments initialized by balanced/imbalanced climatological ICs and the climatological mean IC. Results show that the imbalance is controllable during 7 d prediction. Additionally, errors of 7-d temperature prediction from experiments initialized by balanced ICs dominate when compared to errors from experiment initialized by the imbalanced IC (figures not shown).

4 Discussion and summary

In this study, we identified the sensitive area for targeted ob-

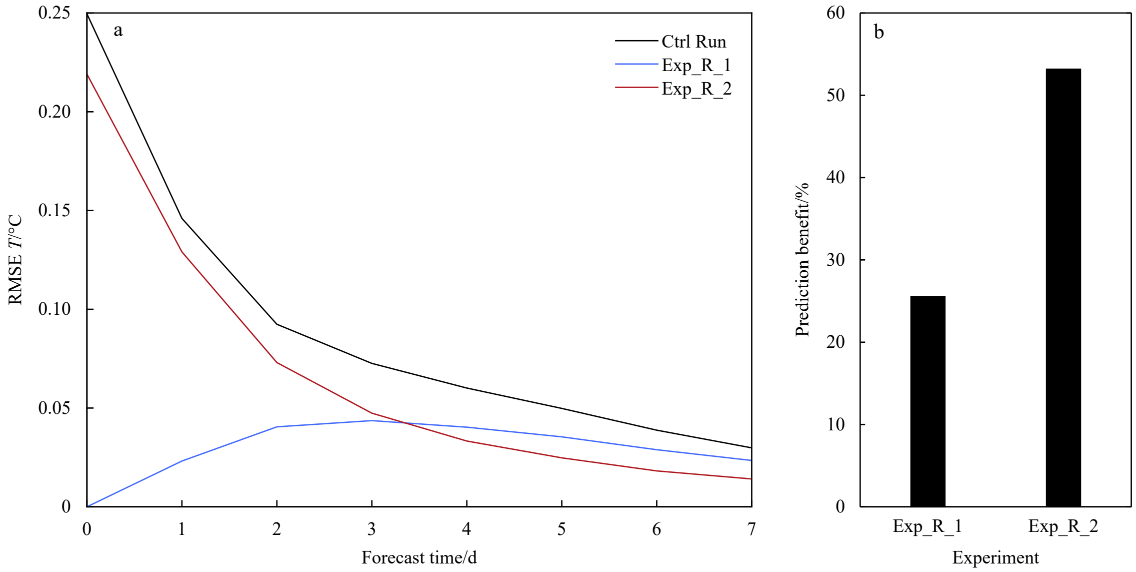

Fig. 7. Temporal evolution of root mean square errors of area-averaged temperature profile over the verification area (a), and corresponding prediction benefits (b) for sensitivity experiments based on removing different initial random errors. Exp_R_1 and Exp_R_2 denote experiment with removing initial random errors from the verification area and sensitive area, respectively. Ctrl Run in a denotes experiment without removing initial errors from any areas.

Table 4. Experimental design of balanced/imbalanced initial conditions (ICs)

Experiment name	IC_mean	IC_23	IC_25	IC_comb
IC	climatological mean of model output from 6th to 25th	model output of the 23rd climatic year	model output of the 25th climatic year	combined ICs from IC_23 and IC_25[1)]

Note: [1)] The ICs are from model output of the 23rd climatic year at the model grid points (i, j) where $(i+j)$ are odd and are from model output of the 25th climatic year at the model grid points (i, j) where $(i+j)$ are even.

servation to improve short-term (7 d) VTS prediction in summer in the Yellow Sea. The sensitive areas were identified based on three different climatologically stable cases. To locate the sensitive areas, the adjoint-free algorithm of CNOP was used with vertically integrated temperature as the guidance. Moreover, the effectiveness of the CNOP-based sensitive area for summertime VTS was investigated through two sets of sensitivity experiments with adding and removing initial random errors of temperature in different areas. Results show that the locations of CNOP-based sensitive areas were generally northeast to the verification area for VTS prediction in summer in the Yellow Sea, which were possibly associated with the southwestward background currents. Initial errors added on the sensitive area have the largest negative effect on the predicted VTS in the verification area at verification time compared to initial errors added on other areas including the verification area itself. Initial errors removed from the identified sensitive area through deploying simulated observations in that area showed more benefits of VTS prediction at the verification time than initial errors that removed from the verification area itself. This indicated that targeted observation in the CNOP-based identified sensitive area is effective for improving short-term VTS prediction in summer in the Yellow Sea. It is worth mentioning that results of the sensitivity experiments shown in this paper do not change if we use Case 1 and Case 2.

In this study, we extended the scope of targeted observation to summertime VTS prediction in the shallow Yellow Sea, and quantitatively evaluated its effectiveness on VTS prediction. However, some future works are still required to make the conclusions obtained in this study more convincing. First, the effectiveness investigated based on the climatological state should be further verified based on hindcast and forecasting. Second, further verification of effectiveness should be performed with the Observing System Simulation Experiments (OSSEs) based on appropriate data assimilation methods and with the Observing System Experiments (OSEs) using real data collected in field campaigns.

Acknowledgement

We thank the super computer at the Navy Submarine Academy Underwater Marine Environment Institute for offering computational resource.

References

Ancell B C, Mass C F. 2006. Structure, growth rates, and tangent linear accuracy of adjoint sensitivities with respect to horizontal and vertical resolution. Monthly Weather Review, 134(10): 2971–2988, doi: 10.1175/MWR3227.1

Baehr J, McInerney D, Keller K, et al. 2008. Optimization of an observing system design for the North Atlantic meridional overturning circulation. Journal of Atmospheric and Oceanic Technology, 25(4): 625–634, doi: 10.1175/2007JTECHO535.1

Bei Naifang, Zhang Fuqing, Nielsen-Gammon J W. 2012. Ensemble-based observation targeting for improving ozone prediction in Houston and the surrounding area. Pure and Applied Geophysics, 169(3): 539–554, doi: 10.1007/s00024-011-0386-z

Bishop C H, Etherton B J, Majumdar S J. 2001. Adaptive sampling with the ensemble transform Kalman filter: Part I. Theoretical aspects. Monthly Weather Review, 129(3): 420–436, doi: 10.1175/1520-0493(2001)129<0420:ASWTET>2.0.CO;2

Chen Guozhen, Niu Yinyi, Wen Shengchang, et al. 1992. Marine Atlas of Bohai Sea, Yellow Sea, East China Sea (Hydrology) (in Chinese). Beijing: China Ocean Press

Chu P C, Wells S K, Haeger S D, et al. 1997. Temporal and spatial scales of the Yellow Sea thermal variability. Journal of Geophysical Research: Oceans, 102(C3): 5655–5667, doi: 10.1029/96JC03428

Duan Wansuo, Li Xuquan, Tian Ben. 2018. Towards optimal observational array for dealing with challenges of El Niño-Southern Oscillation predictions due to diversities of El Niño. Climate Dynamics, 51(9): 3351–3368, doi: 10.1007/s00382-018-4082-x

Duan Wansuo, Mu Mu, Wang Bin. 2004. Conditional nonlinear optimal perturbations as the optimal precursors for El Nino-Southern Oscillation events. Journal of Geophysical Research: Atmospheres, 109(D23): D23105

Hamill T M, Snyder C. 2002. Using improved background-error covariances from an ensemble Kalman filter for adaptive observations. Monthly Weather Review, 130(6): 1552–1572, doi: 10.1175/1520-0493(2002)130<1552:UIBECF>2.0.CO;2

Hu Junya, Duan Wansuo. 2016. Relationship between optimal precursory disturbances and optimally growing initial errors associated with ENSO events: Implications to target observations for ENSO prediction. Journal of Geophysical Research: Oceans, 121(5): 2901–2917, doi: 10.1002/2015JC011386

Hu Huiqin, Sun Juanzhen, Zhang Qinghong. 2017a. Assessing the impact of surface and wind profiler data on fog forecasting using WRF 3DVAR: An OSSE study on a dense fog event over North China. Journal of Applied Meteorology and Climatology, 56(4): 1059–1081, doi: 10.1175/JAMC-D-16-0246.1

Hu Huiqin, Zhang Qinghong, Sun Juanzhen, et al. 2017b. Impact of high-frequency observations on fog forecasting: A case study of OSSE. Tellus A: Dynamic Meteorology and Oceanography, 69(1): 1396182, doi: 10.1080/16000870.2017.1396182

Hu Huiqin, Zhang Qinghong, Xie Baoguo, et al. 2014. Predictability of an advection fog event over North China. Part I: Sensitivity to initial condition differences. Monthly Weather Review, 142(5): 1803–1822, doi: 10.1175/MWR-D-13-00004.1

Huang Ling, Meng Zhiyong. 2014. Quality of the target area for metrics with different nonlinearities in a mesoscale convective system. Monthly Weather Review, 142(7): 2379–2397, doi: 10.1175/MWR-D-13-00244.1

Jin Meibing, Wang Zongshan, Xu Bochang. 1993. Three-dimensional numerical prediction of vertical temperature structure of the Huanghai and the Bohai Seas. Acta Oceanologica Sinica, 12(4): 511–520

Kramer W, Dijkstra H A, Pierini S, et al. 2012. Measuring the impact of observations on the predictability of the Kuroshio extension in a shallow-water model. Journal of Physical Oceanography, 42(1): 3–17, doi: 10.1175/JPO-D-11-014.1

Langland R H. 2005. Issues in targeted observing. Quarterly Journal of the Royal Meteorological Society, 131(613): 3409–3425, doi: 10.1256/qj.05.130

Large W G, McWilliams J C, Doney S C. 1994. Oceanic vertical mixing: a review and a model with a nonlocal boundary layer parameterization. Reviews of Geophysics, 32(4): 363–403, doi: 10.1029/94RG01872

Li Yineng, Peng Shiqiu, Liu Duanling. 2014. Adaptive observation in the South China Sea using CNOP approach based on a 3-D ocean circulation model and its adjoint model. Journal of Geophysical Research: Oceans, 119(12): 8973–8986, doi: 10.1002/2014JC010220

Liang Peng, Mu Mu, Wang Qiang, et al. 2019. Optimal precursors triggering the Kuroshio intrusion into the South China Sea obtained by the conditional nonlinear optimal perturbation approach. Journal of Geophysical Research: Oceans, 124(6): 3941–3962, doi: 10.1029/2018JC014545

MacKinnon J A, Gregg M C. 2003. Mixing on the late-summer New England shelf-solibores, shear, and stratification. Journal of Physical Oceanography, 33(7): 1476–1492, doi: 10.1175/1520-0485(2003)033<1476:MOTLNE>2.0.CO;2

MacKinnon J A, Gregg M C. 2005. Spring mixing: turbulence and internal waves during restratification on the New England shelf. Journal of Physical Oceanography, 35(12): 2425–2443, doi: 10.1175/JPO2821.1

Majumdar S J. 2016. A review of targeted observations. Bulletin of the American Meteorological Society, 97(12): 2287–2303, doi: 10.1175/BAMS-D-14-00259.1

Morss R E, Emanuel K A, Snyder C. 2001. Idealized adaptive observation strategies for improving numerical weather prediction. Journal of the Atmospheric Sciences, 58(2): 210–232, doi: 10.1175/1520-0469(2001)058<0210:IAOSFI>2.0.CO;2

Mu Mu. 2013. Methods, current status, and prospect of targeted observation. Science China Earth Sciences, 56(12): 1997–2005, doi: 10.1007/s11430-013-4727-x

Mu Mu, Duan Wansuo, Chen Dake, et al. 2015. Target observations for improving initialization of high-impact ocean-atmospheric environmental events forecasting. National Science Review, 2(2): 226–236, doi: 10.1093/nsr/nwv021

Mu Mu, Duan Wansuo, Tang Youmin. 2017. The predictability of atmospheric and oceanic motions: retrospect and prospects. Science China Earth Sciences, 60(11): 2001–2012, doi: 10.1007/s11430-016-9101-x

Mu Mu, Duan Wansuo, Wang Bin. 2003. Conditional nonlinear optimal perturbation and its applications. Nonlinear Processes in Geophysics, 10(6): 493–501, doi: 10.5194/npg-10-493-2003

Palmer T N, Gelaro R, Barkmeijer J, et al. 1998. Singular vectors, metrics, and adaptive observations. Journal of the Atmospheric Sciences, 55(4): 633–653, doi: 10.1175/1520-0469(1998)055<0633:SVMAAO>2.0.CO;2

Powell M J D. 1983. VMCWD: A Fortran subroutine for constrained optimization. ACM SIGMAP Bulletin, 32: 4–16

Qin Xiaohao, Mu Mu. 2011. A study on the reduction of forecast error variance by three adaptive observation approaches for tropical cyclone prediction. Monthly Weather Review, 139(7): 2218–2232, doi: 10.1175/2010MWR3327.1

Qiu Daoli. 1982. Characteristic analysis on the daily variation of sea water temperature in the Bohai sea and inshore region of the Huanghai sea and east China Sea. Acta Oceanologica Sinica (in Chinese), 4(4): 391–403

Shchepetkin A F, McWilliams J C. 2005. The regional oceanic modeling system (ROMS): A split-explicit, free-surface, topography-following-coordinate oceanic model. Ocean Modelling, 9(4): 347–404, doi: 10.1016/j.ocemod.2004.08.002

Tan Xiaowei, Wang Dongliang. 2010. Preliminary study of sensitive areas for several tropical cyclone track prediction cases in 2007. Atmospheric and Oceanic Science Letters, 3(6): 299–302, doi: 10.1080/16742834.2010.11446887

Tan Xiaowei, Wang Bin, Wang Dongliang. 2010. Impact of different guidances on sensitive areas of targeting observations based on the CNOP method. Acta Meteorologica Sinica, 24(1): 17–30

Wajsowicz R C. 1993. A consistent formulation of the anisotropic stress tensor for use in models of the large-scale ocean circulation. Journal of Computational Physics, 105(2): 333–338, doi: 10.1006/jcph.1993.1079

Wang Qiang, Mu Mu, Dijkstra H A. 2013. The similarity between optimal precursor and optimally growing initial error in prediction of Kuroshio large meander and its application to targeted observation. Journal of Geophysical Research: Oceans, 118(2): 869–884, doi: 10.1002/jgrc.20084

Wang Bin, Tan Xiaowei. 2009. A fast algorithm for solving CNOP and associated target observation tests. Acta Meteorologica Sinica, 23(4): 387–402

Wen Xixi, Duan Wansuo. 2019. Errors in current velocity in the low-latitude North Pacific: results from the regional ocean modeling system. Advances in Atmospheric Sciences, 36(4): 397–416, doi: 10.1007/s00376-018-8140-4

Wu C C, Chen J H, Lin P H, et al. 2007. Targeted observations of tropical cyclone movement based on the adjoint-derived sensitivity steering vector. Journal of the Atmospheric Sciences, 64(7): 2611–2626, doi: 10.1175/JAS3974.1

Xia Changshui, Qiao Fangli, Yang Yongzeng, et al. 2006. Three-dimensional structure of the summertime circulation in the Yellow Sea from a wave-tide-circulation coupled model. Journal of Geophysical Research: Oceans, 111(C11): C11S03, doi: 10.1029/2005JC003218

Yang Dezhou, Yin Baoshu, Liu Zhiliang, et al. 2011. Numerical study of the ocean circulation on the East China Sea shelf and a Kuroshio bottom branch northeast of Taiwan in summer. Journal of Geophysical Research: Oceans, 116(C5): C05015

Zhang Mengning, Liu Jinfang, Mao Kexiu, et al. 2006. The general distribution characteristics of thermocline of China Sea. Marine Forecasts (in Chinese), 23(4): 51–58

Zhang Kun, Mu Mu, Wang Qiang. 2017. Identifying the sensitive area in adaptive observation for predicting the upstream Kuroshio transport variation in a 3-D ocean model. Science China Earth Sciences, 60(5): 866–875, doi: 10.1007/s11430-016-9020-8

Zhang Kun, Mu Mu, Wang Qiang, et al. 2019. CNOP-based adaptive observation network designed for improving upstream Kuroshio transport prediction. Journal of Geophysical Research: Oceans, 124(6): 4350–4364, doi: 10.1029/2018JC014490

Zhang Kun, Wang Qiang, Mu Mu, et al. 2016. Effects of optimal initial errors on predicting the seasonal reduction of the upstream Kuroshio transport. Deep Sea Research Part I: Oceanographic Research Papers, 116: 220–235, doi: 10.1016/j.dsr.2016.08.008

Zhou Feifan, Zhang He. 2014. Study of the schemes based on CNOP method to identify sensitive areas for typhoon targeted observations. Chinese Journal of Atmospheric Sciences (in Chinese), 38(2): 261–272